J Mater Sci (2017) 52:2222–2231

Electric relaxation and Mn^{3+}/Mn^{4+} charge transfer in Fe-doped $Bi_{12}MnO_{20}$–$BiMn_2O_5$ structural self-composite

A. Leonarska[1], M. Kądziołka-Gaweł[1], A. Z. Szeremeta[1], R. Bujakiewicz-Korońska[2], A. Kalvane[3], and A. Molak[1,*]

[1] *Institute of Physics, University of Silesia, Uniwersytecka 4, 40-007 Katowice, Poland*
[2] *Institute of Physics, Pedagogical University, Podchorążych 2, 30-084 Kraków, Poland*
[3] *Institute of Solid State Physics, University of Latvia, 8 Kengaraga, Riga LV-1063, Latvia*

Received: 29 August 2016
Accepted: 15 October 2016
Published online: 24 October 2016

ABSTRACT

Fe-doped $Bi_{12}MnO_{20}$–$BiMn_2O_5$ ceramics was sintered at 1130 K for 6 h in ambient air. Two centro-symmetric phases formed thermodynamically stable self-composite material that was deduced from X-ray pattern analysis. The lattice parameters were $a = 10.147(8)$ Å—for the cubic *I23* $Bi_{12}MnO_{20}$ phase; and $a = 7.545(4)$ Å, $b = 8.538(1)$ Å, $c = 5.758(3)$ Å—for the orthorhombic *Pbam* $BiMn_2O_5$ phase. The ^{57}Fe Mössbauer spectrum, recorded at room temperature, has shown pure electronic quadrupolar split. The major doublets reflected the occurrence of Fe^{3+} ions distributed in two sites, i.e., octahedral $Fe^{4+}O_6$ and square pyramidal $Fe^{3+}O_5$, with preferential occupation of the pyramidal sites, that was consistent with the *Pbam* phase symmetry. The third doublet resulted from the presence of iron Fe^{3+} in tetrahedral $Fe^{3+}O_4$ coordination and corresponded to a small admixture of the *I23* phase. The DC resistivity $\rho_{DC}(T)$ dependence on temperature has shown thermally activated features, and the value of $E_{a,DC}$ varied in the range of 0.22–0.37 eV. The electric impedance was measured in the $f = 20$ Hz–1 MHz and 100–690 K range. Two electrical relaxations were determined using the electric modulus formalism $M''(T)$. Low-temperature relaxation has shown the temperature-dependent activation energy $E_{A,1} = 0.14$–0.20 eV and characteristic time values of $\tau_{01} = 10^{-10}$–10^{-12} s in 100–200 K range. It was attributed to the charge transfer between Mn^{4+}/Mn^{3+} sites. The other relaxation occurred in the 170–220 K range, and it exhibited the following values: $\tau_{02} = 10^{-11}$ s, and $E_{A,2} = 0.27$ eV. A disorder-related VRH polaron model was proposed for $\rho_{DC}(T)$ and for electric relaxation processes.

Address correspondence to E-mail: andrzej.molak@us.edu.pl

DOI 10.1007/s10853-016-0515-2

Introduction

In recent years, there has been an increasing interest in electromagnetic and electro-optic composite materials due to several promising potential applications in digital memory storage, spintronics, and a wide spectrum of sensor technologies [1]. A large family of oxides, which includes not only perovskites but also more complex structures, e.g., sillenites, has recently attracted interest due to their physical properties and technological applications [2, 3]. Sillenites exhibit various properties such as photorefractivity, photoconductivity, and enhanced velocity of ultrasound wave propagation, and such properties have potential applications. Sillenites, which contain tetrahedrally coordinated transition metal ions, e.g., Fe and Mn, offer tuning of electronic structure and photo-electronic features [4–6].

It is worth to notice that the phases with sillenites structure occur together with other binary phases in various, more complex systems. Manganites, which exhibit mixed Mn^{3+} and Mn^{4+} valence, attract attention due to their magnetic order, high electric permittivity, and possible magneto-electric coupling. The mixed valence can be obtained by deliberate doping with hetero-valence ions. The other opportunity originates from the structures, which contain non-equivalent crystallographic sites.

The synthesis of perovskite symmetry $BiMnO_3$ samples demands high hydrostatic pressure at the sintering stage. When bismuth manganite ceramics is sintered at ambient air pressure, thermal decomposition occurs at ~900 K. The appearance of such meta-stable phases, which exhibit different crystallographic symmetries, has been related to structural defects and internal stresses. Therefore, polymorph forms, $BiMn_nO_m$, have been detected and discussed in literature [7, 8]. For instance, pure submicron $BiMn_2O_5$ particles have been obtained by means of hydrothermal method [9]. $BiMn_2O_5$ shows antiferromagnetic order below $T_{Néel} \sim 40$ K [9–11].

When bismuth manganite ceramics is obtained by standard high-temperature sintering in ambient air pressure, the two-phase compound is crystallized. The analysis of X-ray powder diffraction data has shown that bismuth manganite ceramics exhibit, at room temperature, two centro-symmetric phases: the $BiMn_2O_5$ orthorhombic *Pbam* and sillenite $Bi_{12}MnO_{20}$ cubic *I*23 [12]. The $BiMn_2O_5$ phase remains in thermodynamic equilibrium with $Bi_{12}MnO_{20}$ phase [13–15]. $BiMn_2O_5$ has a structure, which contains octahedrally coordinated Mn^{4+} ions and Mn^{3+} ions located in square pyramids [16, 17], whereas $Bi_{12}MnO_{20}$ contains $Mn^{4+}O_4$ tetrahedrons.

Recently, the novel self-composite term was introduced to describe a material, whose elemental composition is not changed, whereas the local distribution of phases varies [18–20]. Therefore, the $Bi_{12}MnO_{20}$–$BiMn_2O_5$ compound, consisting of two stable phases, can be called a self-composite material.

$Bi_{12}MnO_{20}$ shows the energy gap of ~1.66 [6], which is wider than the $BiMn_2O_5$ energy gap: the calculated $E_{gap} = 1.03$ eV and the indirect band gap of ~0.78 eV [21]. Impedance tests have shown marked dispersion of dielectric permittivity. The step-like anomaly in the low-temperature range corresponded to non-ferroelectric relaxation. The $Bi_{12}MnO_{20}$–$BiMn_2O_5$ compound shows small polaron mechanism of electric conductivity with activation energy value 0.4 eV [12, 22].

The mixed Mn^{3+} and Mn^{4+} valence in several bismuth manganite compounds was related not only to magnetic ordering but also to the small polaron mechanism of conductivity [9, 23]. Moreover, in case of increased structural disorder, the variable range hopping (VRH) of small polaron can manifest in low-temperature ranges [24–28].

Doping with Fe ions can serve as a probe for determination of the local crystal lattice symmetry or environment of the ions in the Fe/Mn sublattice. Such an approach is provided by the Mössbauer spectroscopy. In case of low level doping, <10 %, one can expect occurrence of increased disorder in the Fe-doped manganites, while the crystal lattice remains iso-structural with symmetry of the parent material [14, 29–33].

The aim of this work was to characterize structural and electrical features of Fe-doped $Bi_{12}MnO_{20}$–$BiMn_2O_5$ ceramics. We have chosen bismuth manganite ceramics doped with 5 wt% of Fe, which has been produced by standard high-temperature sintering, in the laboratory in Riga University. The sintering conditions were slightly different from those applied for pure $Bi_{12}MnO_{20}$–$BiMn_2O_5$ ceramics sintered formerly [12, 15]. Mössbauer spectroscopy could confirm the symmetry of the Fe ions environment and structural disorder, deduced from XRD analysis. Moreover, we tried to correlate the small polaron models of electric conduction and the presumed occurrence of electrical relaxation to the

charge transfer and structural disorder related to the self-composite features.

Experimental details

Sintering

Fe-doped bismuth manganite ceramics was prepared by standard high-temperature dry sintering method. The chemicals from Aldrich were used: Bi_2O_3 (99.5 %), MnO_2 (99.5 %), and Fe_2O_3 (purity 99.5 %). The Bi_2O_3 and MnO_2 powders were weighed in accordance to chemical formula stoichiometry, and 5 % of Fe_2O_3 was added. The components were mixed in ethanol and homogenized in an agate ball-mill for 24 h. After drying at 400 K, they were calcined for 2 h. Then the calcined powders were ground, pressed under the pressure of 15 MPa at room temperature in the form of pellets having 8 mm in diameter, and sintered for 6 h at $T_S = 1130$ K, in ambient air. The samples in form rectangular plates were cut off for electrical measurements. The powder samples were prepared for the XRD and Mössbauer tests. The powdered sample was additionally annealed and/or sintered at $T_A = 1130$ K for 8 h in an open-tube quartz oven, to control the stability of the structure.

X-ray diffraction test

The powdered sample was studied using a powder diffractometer (Kristalloflex-4, SIEMENS), using filtered CuK_α radiation ($\lambda = 0.154056$ nm; $U = 25$ kV; $I = 15$ mA) and the θ–θ scan technique. The diffraction pattern was collected in the 2θ range (20°–100°) with scan step of 0.02°, and the time count was 15 s for each point, at the room temperature of $T \approx 300$ K. The intensity and position of each measured line were fitted using the least squares method, by means of the X-ray Reflection Profiler software [34]. The crystal structure refinement was performed with the Rietveld profile method using the FullProf software [35]. The occurrence of two phases, *I23* (No. 197) and *Pbam* (No. 55), was checked for the powdered sample [12].

Dielectric impedance

Impedance was measured in $f = 20$ Hz–1 MHz and 100–690 K ranges. The samples—in the form the platelet capacitor, with Ag electrodes—were suspended on two silver wires. Electric capacitance C, conductance G, and resistance R_{DC} were measured using a LCR metre (Wayne Kerr 4300). The DC electric resistance R_{DC} was measured in 200–690 K range, at the measuring voltage of $U_{DC} = 1$ V. The measurements were conducted on heating and cooling at the constant rate of 2 K min^{-1}, using an Unipan 680 temperature controller. The results were analysed with the use of electric modulus formalism $M^*(T,f) = (\varepsilon^*)^{-1} = M' + M''$, where ε^*—dielectric permittivity; M', M''—real and imaginary part of electric modulus, respectively.

Mössbauer spectroscopy

The sample was ground into powder and prepared in the shape of a thin disc. The ^{57}Fe Mössbauer spectrum was recorded at room temperature using a constant acceleration spectrometer with ^{57}Co:Cr source, a multichannel analyser with 1024 channels and linear arrangement of the ^{57}Co source, an absorber, and a detector. The values of isomer shifts (IS) and quadrupole splitting (QS), for all identified sub-spectra, were determined with reference to the centroid of the spectrum of a standard α-Fe foil. The numerical analysis of the Mössbauer spectrum was performed with the use of WMOSS program.

Results

XRD determination of the crystal structure

The XRD pattern lines have been successfully identified using the two sets of indices listed in our previous paper, concerning bismuth manganite ceramics [12]. The analysis of X-ray powder diffraction data (Fig. 1a) allowed us to confirm that the Fe-doped bismuth manganite ceramics consists of two centrosymmetric phases: the orthorhombic *Pbam* (No. 55) [14, 16, 17, 31] and the sillenite cubic *I23* (No. 197) [2, 6]. The cubic sillenite structure of $Bi_{12}MnO_{20}$ phase can be described as discrete $M^{4+}O_4$ tetrahedrons (M = Mn or Fe) separated by bismuth-oxygen framework. In case of the orthorhombic $BiMn_2O_5$ phase, the $M^{4+}O_6$ octahedrons form linear chains and the square pyramids $M^{3+}O_5$ interconnect the octahedrons via oxygen ions. In accordance to literature

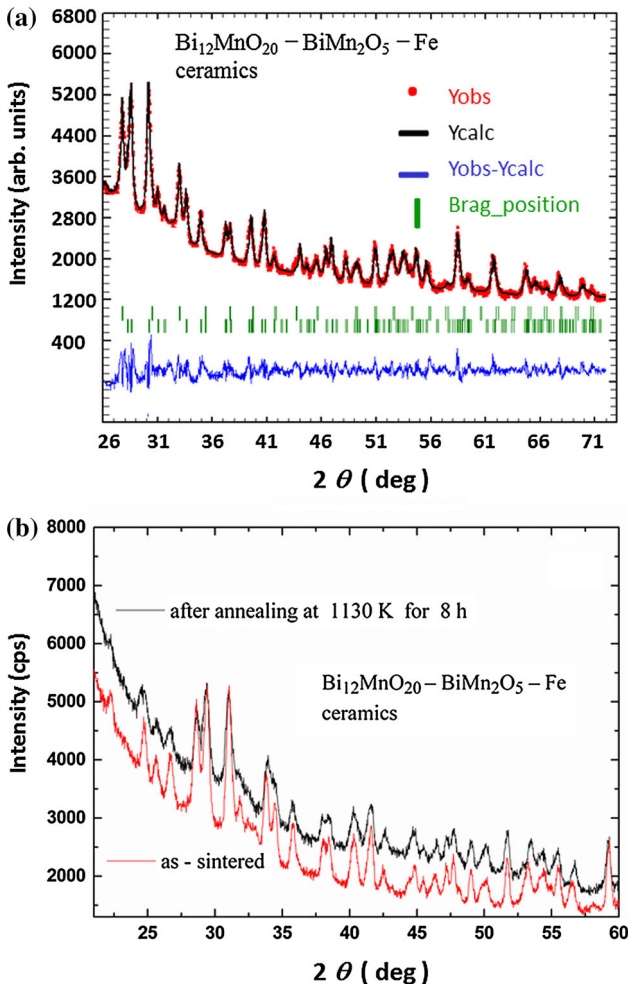

Figure 1 **a** X-ray powder diffraction pattern of $Bi_{12}MnO_{20}$–$BiMn_2O_5$–Fe ceramics obtained at room temperature: experimental (*circles*) and calculated (*continuous line*) spectrum; *vertical ticks* show 2θ Bragg positions, the *curve* at the *bottom* shows the difference between experimental pattern; and spectrum calculated for the superposition of *Pbam* and *I23* space groups. **b** The XRD patterns obtained for the as sintered sample and for the sample after annealing at 1130 K for 8 h.

data, we presumed that Fe ions randomly replace Mn ions [29, 31, 32].

The analysis of the room temperature XRD data of Fe-doped bismuth manganite shows the following superstructure: $\left(2\sqrt{2a_p} \times 2\sqrt{2a_p} \times 2\sqrt{2a_p}\right)$ for *I23* phase, and $\left(2a_p \times 2b_p \times \sqrt{2c_p}\right)$ for *Pbam* phase. Atoms are shifted from their ideal positions (see x, y, and z values in Table 1), which corresponds to deformation or distortion of the unit cell. Crystal lattice parameters for these phases are shown in Table 1.

The occurrence of two stable phases was not affected by the additional sintering conducted at $T_A = T_S = 1130$ K for 8 h, because of the set of diffraction lines remaining in the XRD pattern (Fig. 1b). However, the line placed at ~32° in the XRD pattern vanished. We deduce that a residual amount of additional compound, resulting probably from not fully reacted substrates, most likely bismuth carbonate $(BiO)_2CO_3$, that were removed after the sample was thermally treated [15, 36, 37]. Moreover, the disorder increased slightly, since the FWHM of the (112) line from *Pbam* symmetry and (400) line from *I23* symmetry, e.g., placed at 35.77(2)° changed by 0.08.

Mössbauer study

In accordance to literature data, Fe ions randomly replace Mn ions in the manganite structures [29–32]. Mössbauer spectroscopy provides an insight to the local structure that enabled us to verify the variety of Fe environments in the $Bi_{12}MnO_{20}$–$BiMn_2O_5$ self-composite.

The ^{57}Fe Mössbauer spectrum at room temperature is shown in Fig. 2, and the hyperfine parameters derived from the fitting procedure are collected in Table 2. This spectrum shows pure electronic quadrupolar interactions. It was fitted with three paramagnetic doublets. The observed isomer shift values are characteristic for Fe^{3+} ions placed at all sites. The QS observed in the Mössbauer spectrum, corresponds to the asymmetrical part of the electronic hyperfine interaction between the iron nucleus and its surrounding charges. Doublets labelled 1 and 2 represent iron Fe^{3+} ions distributed in the two sites of the $BiMn_2O_5$ structure, octahedral one and square pyramidal one, with a preferential occupation of the octahedral site (see Table 2). The isomer shift values of these two doublets are comparable with those presented in literature [30]. The quadrupole splitting value obtained for the octahedral site, QS = 1.131 mm s^{-1}, is close to that of Fe-doped $BiMnO_3$ (1.18 mm s^{-1}) [30]. The large QS value indicates strong Jahn–Teller distortion of the octahedrons.

There is a third doublet with hyperfine parameters, visible in the Mössbauer spectrum. It originates from a small admixture of another crystal phase with iron Fe^{3+} in tetrahedral coordination. It can be related to the $Bi_{12}MnO_{20}$ phase.

Thus, the Mössbauer test confirmed the occurrence of three types of sites in the studied ceramics. The

Table 1 Crystal lattice parameters, a, b, and c, obtained for $Bi_{12}MnO_{20}$–$BiMn_2O_5$–Fe ceramics powdered sample, from the refinement of XRD pattern, measured at $T = 300$ K

Phase I: *I23* (No. 197) space group $a = 10.147$ (8) [Å] $R_{Bragg} = 6.33$ %					Phase II: *Pbam* (No. 55) space group $a = 7.545$ (4) [Å], $b = 8.538$ (1) [Å], $c = 5.758$ (3) [Å] $R_{Bragg} = 9.42$ %				
Atom	x	y	z	B^{iso} [Å]^2	Atom	x	y	z	B^{iso} [Å]^2
Bi (24*f*)	0.132 (4)	0.425 (8)	0.001 (2)	0.985 (3)	Bi (4*g*)	0.175 (6)	0.181(3)	0	0.627 (8)
Mn/Fe (2*a*)	0	0	0	0.785 (2)	Mn/Fe (4*f*)	0.5	0	0.236 (4)	0.541 (7)
					Mn/Fe (4*h*)	0.349 (3)	0.302(5)	0.5	0.541 (7)
O1 (24*f*)	0.105 (3)	0.262 (9)	0.490 (1)	1.214 (3)	O1 (4*e*)	0	0	0.452 (8)	0.842 (4)
O2 (8*c*)	0.167 (5)	0.167 (5)	0.167 (5)	1.214 (3)	O2 (8*i*)	0.432 (6)	0.238(4)	0.358 (2)	0.842 (4)
O3 (8*c*)	0.937 (9)	0.937 (9)	0.937 (9)	1.214 (3)	O3 (4*h*)	0.194 (2)	0.434(1)	0.5	0.842 (4)
					O4 (4*g*)	0.214 (3)	0.461(8)	0	0.842 (4)

The x, y, and z are atomic positions in Wyckoff notation. The reliability factors are also given

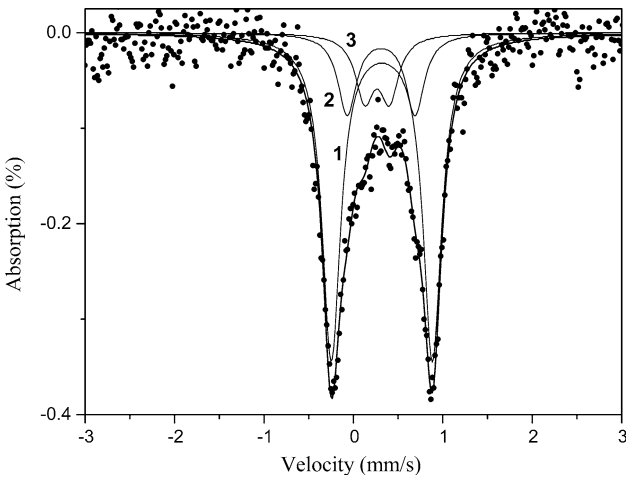

Figure 2 ^{57}Fe Mössbauer spectrum of $Bi_{12}MnO_{20}$–$BiMn_2O_5$–Fe ceramics, obtained at room temperature. The fitted sub-spectra are presented in the spectrum.

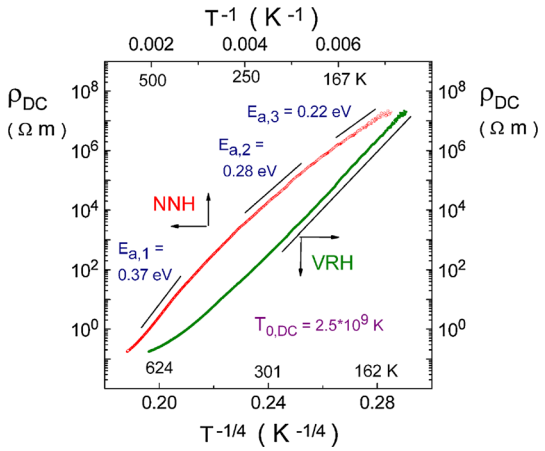

Figure 3 Electric resistivity ρ_{DC} versus $T^{-1/4}$ and ρ_{DC} versus T^{-1} plots. The accuracy of E_a estimation is ±0.01 eV.

octahedral, pyramidal, and tetrahedral sites correspond to the $Bi_{12}MnO_{20}$ and the $BiMn_2O_5$ structures of the self-composite determined using XRD analysis.

Electric properties

The resistivity ρ_{DC} decreased with increasing temperature that indicated thermally activated electric conductivity. It should be noted that several compounds containing Mn ions show polaronic conduction [12, 23, 24, 27, 28, 38, 39]. There are two models of small polaron conductivity, which include the potential energy landscape determined by the degree of crystal lattice disorder [25, 26]. Nearest-neighbours hopping (NNH) occurs for ordered solids and the Arrhenius law is fulfilled

$$\rho = \rho_0 \exp(E_a/k_B T). \quad (1a)$$

Solids disordered, at least locally, show deviation from the Arrhenius law. In such a case, VRH of small polaron occurs [24]

$$\rho = \rho_0 \exp[(T_0/T)^{1/4}], \quad (1b)$$

where the parameter T_0 denotes Mott temperature and is measure of disorder, exponent equals to ¼ in case of three-dimensional conductivity. Moreover, T_0 relates to density of states in the vicinity of Fermi level, N (E_F).

The $Bi_{12}MnO_{20}$–$BiMn_2O_5$–Fe ceramics has shown structural disorder; hence both models were checked. The ρ_{DC} temperature dependence was shown both in the ρ_{DC} versus T^{-1} plot, which corresponds to the NNH of small polaron, and in the ρ_{DC} versus $T^{-1/4}$

Table 2 Mössbauer hyperfine parameters of the investigated compound

Doublet no.	IS (mm/s)	QS (mm/s)	G (mm/s)	A (%)	Site symmetry
1	0.318	1.131	0.26	69	Octahedral
2	0.310	0.759	0.26	17	Pyramidal
3	0.264	0.277	0.26	14	Tetrahedral

IS isomer shift, *QS* quadruple splitting, *G* full width at half maximum of the fitted line, *A* relative intensity

plot, which corresponds to the VRH small polaron model (Fig. 3).

In case of Arrhenius plot, the experimental points in the ρ_{DC} (T^{-1}) plot were not aligned in a straight line that corresponded to the monotonic change in E_a value. Therefore, one could not determine the same value of activation energy in the whole temperature range. The activation energy values were estimated in narrower ranges: $E_{a,1} = 0.37$ eV (coefficient of determination, $R^2 = 0.9996$) in 358–568 K; $E_{a,2} = 0.28$ eV ($R^2 = 0.9996$) in 197–253 K; $E_{a,3} = 0.22$ eV ($R^2 = 0.9956$) in 151–173 K, respectively.

The use of the VRH model, $\rho_{DC} = \rho_0 \exp[(T_{0,DC}/T)^{1/4}]$, allowed us to determine that it is applicable below ~300 K (see the straight-line segment in Fig. 3). The value $T_{0,DC} = 2.5 \times 10^9$ K ($R^2 = 0.9999$) was determined. Hence, the VRH of small polaron model fitted the resistivity with higher accuracy in the low-temperature range (compare R^2 values). Such a result was consistent with the structural disorder of the studied structural $Bi_{12}MnO_{20}$–$BiMn_2O_5$–Fe self-composite.

In case of lossy or conductive dielectric materials, the measured permittivity is the sum of three components:

$$\varepsilon_{measured}(\omega) = \varepsilon(\omega) + \sigma_h(\omega)/\varepsilon_0\omega + (i\,\sigma_{DC})/(\varepsilon_0\omega), \quad (2)$$

where ε (ω) is dielectric permittivity, σ_h is AC conductivity related to charge carriers hopping, and σ_{DC} is DC conductivity contribution [40]. The same data can also be shown in the electric modulus representation, $M^* = (\varepsilon^*)^{-1} = M' + M''$. In this representation, the increase of losses in low-frequency range, related to conductivity, $\varepsilon'' \sim \sigma\omega^{-1}$, is transformed into the relaxation peak in the $M''(\omega)$ spectra. This transformation allows us to discern dipole relaxations covered in the dielectric loss ε'' spectra by the conductivity part [41–43].

The dielectric permittivity, $\varepsilon^*(T,\omega)$, of the studied ceramics reached values of the order of 10^4 when it was measured in high-temperature range. It was

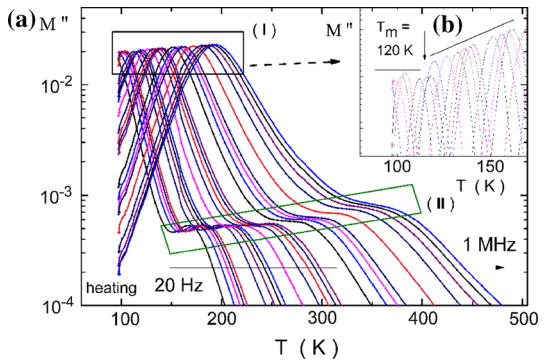

Figure 4 **a** Imaginary part of electric modulus $M''(T,f)$ versus temperature T for the $Bi_{12}MnO_{20}$–$BiMn_2O_5$–Fe ceramics, shown for the 90–500 K range. The *inset* (**b**) shows M'' temperature dependence related to the relaxation process (I), which occurs in the 90–200 K range.

dominated by conductivity contribution. Therefore, the imaginary part of electric modulus $M^*(T,f)$ temperature dependence for $Bi_{12}MnO_{20}$–$BiMn_2O_5$–Fe has been shown (Fig. 4). There are two different anomalies in $M''(T)$ dependence, marked by frames. These anomalies shift toward higher temperatures with increasing frequencies, and hence, they can be assigned to relaxation processes. The most probable relaxation times, $\tau = (2\pi f_{max})^{-1}$, were estimated from the M'' peak coordinates.

One process (I) occurs in the 90–200 K range. The details of this peak anomaly are shown in the inset (Fig. 4b). The $M''(T)$ peak amplitude is constant in the 90–120 K range and increases in the 120–200 K range. The other process (II) occurs in the ~170–400 K range. However, the explicit peak in the $M''(T)$ dependence occurs only in the narrower range, ~170–220 K, and a step-like anomaly manifests at higher temperature.

The relaxation times relate to conductivity for many disordered solids via the Barton–Nakajima–Namikawa (BNN) relation [26]:

$$\omega* = \sigma_{DC}/p\varepsilon_0\Delta\varepsilon, \quad (3)$$

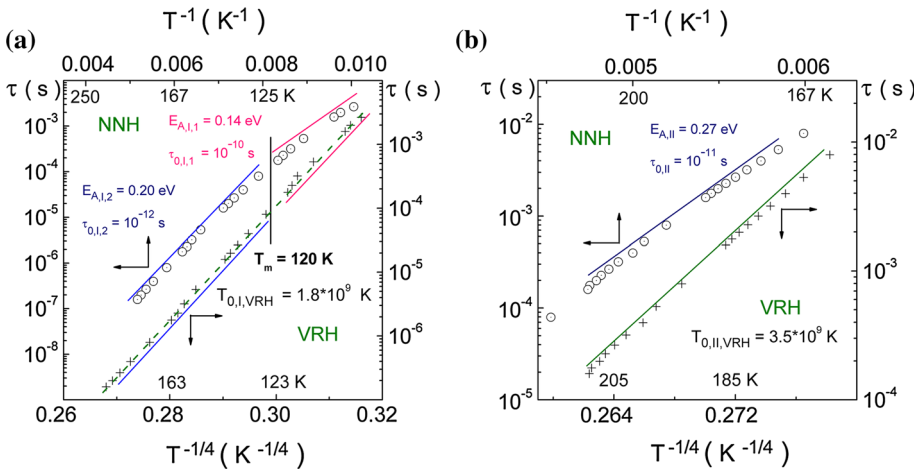

Figure 5 Thermally activated nearest-neighbour hopping of small polaron and variable range hopping polaron models fitted for the relaxation time–temperature dependences. Relaxation times related to process (I) is shown in graph (**a**) while that related to process (II) in graph (**b**).

where ω^* is the frequency marking the onset of AC conduction, σ_{DC} is the DC conductivity, p is the constant of the order of unity, and $\Delta\varepsilon$ is the dielectric strength, i.e., the difference between static and high-frequency relative dielectric permittivity.

The most probable relaxation times were estimated from the peak coordinates in the $M''(T,f)$ dependence, $\tau = 1/2\pi f$. We presumed that the relaxation times would reflect the structural disorder, in accordance to the BNN relation, $\tau\ (T) = \xi\ \rho_{DC}(T)$. Therefore, the relaxation times were plotted in temperature scales appropriate for the NNH and the VRH models. The relaxation times related to processes (I) and (II) are shown in Fig. 5a and b, respectively. The numerical fit was performed in the same temperature ranges for adequate comparison, both for the NNH dependence, $\tau\ (T^{-1})$, and the VRH dependence, $\tau\ (T^{-1/4})$.

In case of process (I), the relaxation times were fitted, in accordance to thermally activated NNH hopping of small polaron, to Arrhenius law: $\tau = \tau_0$ exp (E_A/kT). Activation energy values changed from $E_{A,I,1} = 0.14$ eV in the 90–120 K range to $E_{A,I,2} = 0.20$ eV in the 125–200 K range. The cross-over in the activation energy at $T = 120$ K (see Fig. 5a) corresponded to the temperature T_m where an offset in modulus amplitude manifests (compare Fig. 4b). The characteristic time values were $\tau_{0,I,1} = 10^{-10}$ s and $\tau_{0,I,2} = 10^{-12}$ s, respectively. We would like to mention that a nonlinear dependence in the relaxation times in the Arrhenius plot could be distinguished, which reflected in the E_A value change. Such a curve indicated that activation energy depended on temperature, and the variable range hopping of small polaron model could be concerned [28, 42, 43]. Therefore, the most probable relaxation times have been also fitted in accordance to the VRH of small polaron model: $\tau = \tau_0$ exp $[(T_0/T)^{1/4}]$. The common value, $T_{0,I,VRH} = 1.8 \times 10^9$ K, was determined for both temperature ranges.

The high-temperature anomaly (II) in $M''(T,f)$ plots occurred in the 170–400 K range (see Fig. 4a). However, the determination of the most probable relaxation times, related to the peak position in the $M''(T,f)$ plot, was effective only in the 170–220 K range (Fig. 5b). The determined relaxation times were fitted in accordance to the thermally activated dependence presumed for the nearest-neighbour hopping of small polaron model. The activation energy value was $E_{A,II} = 0.27$ eV, and the characteristic time was $\tau_{0,II} = 10^{-11}$ s. Consequently, the VRH polaron model was also applied to this relaxation process (see Fig. 5b). The value $T_{0,II,VRH} = 3.5 \times 10^9$ K was determined.

It would be noticed that the fitting performed in accordance to the VRH of small polaron model has shown better accuracy [$R^2 = 0.9948$ in the 90–120 K range and $R^2 = 0.9995$ in the range of 125–200 K for process (I) and $R^2 = 0.9997$ for process (II)], than the accuracy determined from fitting performed for the NNH of polaron model [$R^2 = 0.9944$ and $R^2 = 0.9988$ for the process (I) and $R^2 = 0.9981$ for the process (II)], respectively. Therefore, we deduce that relaxation times reflect a structural disorder.

Discussion

Fe-doped $Bi_{12}MnO_{20}$–$BiMn_2O_5$ ceramics was prepared by high-temperature sintering in air, at slightly different sintering temperature and time, in comparison to the non-doped $Bi_{12}MnO_{20}$–$BiMn_2O_5$

samples [12, 39]. Despite this difference, the XRD patterns exhibited the occurrence of the cubic *I23* $Bi_{12}MnO_{20}$ phase and orthorhombic *Pbam* $BiMn_2O_5$ phases, for both the non-doped and Fe-doped samples. These phases remained in thermodynamic equilibrium and their ratio depended slightly on the temperature and time of sintering [13–15]. The superstructure lines occurred in XRD pattern for both phases. Such an effect corresponded to the crystal lattice deformation or distortion (the parameters of unit cells are listed in Table 1). The obtained values of the refinement parameters suggested the presence of structural disorder. This effect might correspond to the unit cells, which consist of tetrahedrons, octahedrons, and square pyramids.

It should be noted that "bismuth manganite" denotes the general content of the elements [39] and not the true local composition. Moreover, our research has shown different symmetries of the two determined phases, in contrary to the $BiMnO_3$–Fe samples produced under high hydrostatic pressure by Belik et al. [8, 30, 33].

The Mössbauer spectroscopy study confirmed the variance in the surrounding of Fe^{3+} ions. The Fe^{3+} ions accommodated preferentially in the FeO_6 octahedrons (~70 %). The minor amount placed in the pyramids FeO_5 and FeO_4 tetrahedrons. It has been shown by Retuerto et al. [31] that Fe ions preferentially occupy the pyramidal $Fe^{3+}O_5$ sites; however, the disorder related to anti-site occupancy of the octahedral sites was also determined in the $BiMn_2O_5$ compound. It should be noticed that the occurrence of Fe^{3+} ions in the octahedral and tetrahedral environments needed charge compensation when they replaced manganese ions in the $Mn^{4+}O_6$ and $Mn^{4+}O_4$ units. The charge compensation could be fulfilled by the induced oxygen vacancies, V_O, in such cases.

We presume that structural and chemical non-homogeneity provides the necessary background for the occurrence of dielectric dispersion and relaxation. One possibility might originate from the misfit strains induced by different radii of the Fe and Mn ions and also induced by interfaces, which are formed between the structures of the two phases with different symmetries. The more plausible possibility corresponds to the Mn^{4+}, Mn^{3+}, and Fe^{3+} charge states, randomly distributed in oxygen tetrahedrons, octahedrons and square pyramids. The formation of either Fe^{3+}–V_O or/and of Fe^{3+}–$Mn^{3+/4+}$ pairs in the crystal lattice also can increase local disorder. The O 2p states hybridize with Mn 3d and Fe 3d states, which form the valence band. Therefore, a disordered environment of Mn and Fe ions can affect the electric transport features.

The permittivity relaxor-like dispersion is different from the ferroelectric mechanism [23, 27, 28, 38, 39]. It would be noticed that two relaxation processes occurred also in the non-doped $Bi_{12}MnO_{20}$–$BiMn_2O_5$ self-composite [12]. The low-temperature relaxation has shown $E_A = 0.20$ eV and characteristic time $\tau_0 = 1.8 \times 10^{-12}$ s. The high-temperature relaxation has shown $E_A = 0.24$ eV and $\tau_0 = 1.5 \times 10^{-8}$ s. The low values of activation energy are consistent with polaron hopping.

The manifestation of VRH polaron mechanism of conductivity, in the low-temperature range, indicated a significant role of the structural and chemical disorder, related to the occurrence of two phases and additionally affected by doping with Fe ions. Therefore, we propose that low-temperature relaxation (I) relates to charge hopping or charge transfer between the Mn^{3+} and Mn^{4+} sites.

We would also like to comment upon the dielectric anomaly visible in the $M''(T,f)$ spectrum in the vicinity of 120 K (see Fig. 4). One may note the vague coincidence between this dielectric anomaly and magnetic phase transition, reported in literature. The antiferromagnetic transition at $T_{Néel} = 110$ K for $BiMnO_3$ [44] and ferromagnetic cluster-like behaviour below $T_C = 100$–110 K for Fe-doped $BiMnO_3$ [8, 33] have been reported for these materials, which have shown perovskite symmetry and composition. The antiferromagnetic order below $T_{Néel} = 40$ K has been reported for $BiMn_2O_5$ polycrystalline samples [10]. The ceramics obtained from $NaNbO_3$ mixed with the $Bi_{12}MnO_{20}$–$BiMn_2O_5$ compound also exhibited magnetic ordering below 40 K, most probably related to the $BiMn_2O_5$ phase contribution [45]. On the other hand, a dielectric anomaly has been induced in the $BiMn_{1-x}Ti_xO_5$ compound at ~120 K by Ti ions substitution [11]. Hence, we deduce that the anomaly visible in the $M''(T,f)$ spectrum originated from non-magnetic defects.

Conclusions

We note that electric conductivity dispersion and relaxation corresponds to the disorder related to a variety of structural items in Fe-doped $Bi_{12}MnO_{20}$–

$BiMn_2O_5$ self-composite. The split of the Mössbauer spectrum enabled us to determine the Fe^{3+} sites with tetrahedral, octahedral, and square pyramidal symmetry. The occurrence of these three environments corresponds to the variable range hopping of small polaron model, which was fitted successively in low-temperature range. Oxygen vacancies can provide conditions for charge compensation of Fe^{3+} ions, which replace Mn^{4+} ions. Electric relaxation was attributed to charge transfer between the Mn^{3+} and Mn^{4+} sites. Hence, such electric transport features are consistent with structural disorder, which was identified with the use of XRD and the Mössbauer spectroscopy studies.

Compliance with ethical standards

Conflict of Interest We declare that there are no conflicts of interests. There were no research grants or funds from external companies. The work has been performed in accordance to our duties in the University of Silesia and Pedagogical University.

Open Access

References

[1] Han JT, Huang YH, Wu XJ, Wu CL, Wei W, Peng B, Huang W, Goodenough JB (2006) Tunable synthesis of bismuth ferrites with various morphologies. Adv Mater 18:2145–2148

[2] Valant M, Suvorov D (2002) A stoichiometric model for sillenites. Chem Mater 14:3471–3476

[3] Xiong Y, Wu M, Peng Z, Jiang N, Chen Q (2004) Hydrothermal synthesis and characterization of $Bi_2Fe_4O_9$ nanoparticles. Chem Lett 33:502–503

[4] Hur N, Park S, Sharma PA, Ahn JS, Guha S, Cheong SW (2004) Electric polarization reversal and memory in a multiferroic material induced by magnetic fields. Nature 429:392–395

[5] Nippolainen E, Kamshilin AA, Prokofiev VV, Jaaskelainen T (2001) Combined formation of a self-pumped phase-conjugate mirror and spatial subharmonics in photorefractive sillenites. Appl Phys Lett 78:859–861

[6] Wang Y, He R, Yang M, Wen T, Zhang H, Liang J, Lin Z, Wang Y, Li G, Lin J (2012) Hydrothermal growths, optical features and first-principles calculations of sillenite-type crystals comprising discrete MO_4 tetrahedra. CrystEngComm 14:1063–1068

[7] Montanari E, Righi L, Calestani G, Migliori A, Gilioli E, Bolzoni F (2005) Room temperature polymorphism in metastable $BiMnO_3$ prepared by high-pressure synthesis. Chem Mater 17:1765–1773

[8] Belik AA (2012) Polar and nonpolar phases of $BiMnO_3$: a review. J Solid St Chem 195:32–40

[9] Jia R-J, Han J-T, Wu X-J, Wu C-L, Huang Y-H, Huang W (2008) Controllable synthesis and magnetic property of $BiMn_2O_5$ crystals. Mater Res Bull 43:1702–1708

[10] Liu Q, Sallagoity D, Josse M, Toulemonde O (2013) On the anomalous magnetic behavior and the multiferroic properties in $BiMn_2O_5$. Inorg Chem 52:7853–7861

[11] Shukla DK, Mollah S, Kumar R, Thakur P, Chae KH, Choi WK, Banerjee A (2008) Effect of Ti substitution on multiferroic properties of $BiMn_2O_5$. J Appl Phys 104:033707-1–03370710

[12] Molak A, Leonarska A, Szeremeta A (2015) Electric current relaxation and resistance switching in non-homogeneous bismuth manganite. Ferroelectrics 486:161–172

[13] Sedmidubský D, Leitner J, Beneš O (2006) Phase equilibria modeling in Bi_2O_3–SrO–MnO_x system. CALPHAD 30:179–184

[14] Huo G, Gu Z, Qiu M (2004) Phase relations in the Bi_2O_3–Fe_2O_3–MnO_y system at room temperature. J Alloy Compd 381:317–319

[15] Pilch M, Molak A, Koperski J, Zajdel P (2016) Influence of nitrogen flow during sintering of bismuth manganite ceramics on grain morphology and their surface disorder. Phase Transit. doi:10.1080/01411594.2016.1219737

[16] Nguyen N, Legrain M, Ducouret A, Raveau B (1999) Distribution of Mn^{3+} and Mn^{4+} species between octahedral and square pyramidal sites in $Bi_2Mn_4O_{10}$—type structure. J Mater Chem 8:731–734

[17] Munoz A, Alonso JA, Casais MT, Martinez-Lope MJ, Martinez JL, Fernandez-Diaz MT (2002) Magnetic structure and properties of $BiMn_2O_5$ oxide: a neutron diffraction study. Phys Rev B 65:144423-1–144423-8

[18] Mohaideen KK, Joy PA (2012) Enhancement in the magnetostriction of sintered cobalt ferrite by making self-composites from nanocrystalline and bulk powders. ACS Appl Mater Interfaces 4:6421–6425

[19] Bhowmik RN, Panda MR, Yusuf SM, Mukadam MD, Sinha AK (2015) Structural phase change in $Co_{2.55}Fe_{0.75}O_4$ spinel oxide by vacuum annealing and role of coexisting CoO phase on magnetic properties. J Alloy Compd 646:161–169

[20] Zhang J, Zuo R (2016) A novel self-composite property-tunable $LaTiNbO_6$ microwave dielectric ceramics. Mat Res Bull 83:568–572

[21] Zhang J, Xu B, Li XF, Yao KL, Liu ZL (2011) Origin of the multiferroicity in $BiMn_2O_5$ from first–principles calculations. J Magn Magn Mater 323:1599–1605

[22] Goian V, Kamba S, Savinov M, Nuzhnyy D, Borodavka F, Vanek P, Belik AA (2012) Absence of ferroelectricity in $BiMnO_3$ ceramics. J Appl Phys 112:074112-1–074112-6

[23] Dar MS, Akram KB (2014) Evidence of variable range hopping (VRH) and exchange interaction in Co-doped multiferroic $BiMnO_3$ nanoparticles. J Supercond Nov Magn 27:613–623

[24] Hunt A (1991) The ac conductivity of variable range hopping systems such as amorphous-semiconductors. Philos Mag B 64:579–589

[25] Wubbenhorst M, Turnhout J (2002) Analysis of complex dielectric spectra. I. One-dimensional derivative techniques and three-dimensional modeling. J Non-Cryst Solids 305:40–49

[26] Dyre JC, Maass P, Roling B, Sidebottom DL (2009) Fundamental questions relating to ion conduction in disordered solids. Rep Prog Phys 72:046501-1–04650115

[27] Pal S, Banerjee A, Chatterjee P, Chauduri BK (2003) Evidence of non-adiabatic conduction in $Bi_{0.1}A_{0.9}MnO_3$ (A=Ca, Sr, Pb). Phys Status Solid B 237:513–522

[28] Volkov NV, Eremin EV, Sablina KA, Sapronova NV (2010) Dielectric properties of a mixed-valence $Pb_3Mn_7O_{15}$ manganese oxide. J Phys 22:375901-1–375901-6

[29] Yang T, Abakumov AM, Hadermann J, Van Tendeloo G, Nowik I, Stephens PW, Hemberger J, Tsirlin AA, Ramanujachary KV, Lofland S, Croft M, Ignatov A, Sun J, Greenblatt M (2010) $BiMnFe_2O_6$, a polysynthetically twinned *hcp* MO structure. Chem Sci 1:751–762

[30] Belik AA, Hayashi N, Azuma M, Muranaka S, Takano M, Takayama-Muromachi E (2007) Magnetic and Mössbauer studies of 5 % Fe–doped $BiMnO_3$. J Solid State Chem 180:3401–3407

[31] Retuerto M, Martinez-Lope MJ, Krezhov K, Fernández-Díaz MT, Alonso JA (2011) Structural and magnetic characterization of $BiFe_xMn_{2-x}O_5$ oxides (x = 0.5, 1.0). J Solid State Chem 184:2428–2433

[32] Selbach SM, Tybell T, Einarsrud MA, Grande T (2009) Structure and properties of multiferroic oxygen hyperstoichiometric $BiFe_{1-x}Mn_xO_{3+\delta}$. Chem Mater 21:5176–5186

[33] Belik AA, Takayama-Muromachi E (2007) Effects of isovalent substitution in the manganese sublattice on magnetic, thermal, and structural properties of $BiMnO_3$: $BiMn_{1-x}O_3$ (M = Al, Sc, Cr, Fe, Ga; $0 \le x \le 0.2$). Inorg Chem 46:5585–5590

[34] Kachel A (1995) XP Program Guide

[35] Rodriguez–Carvajal J (2006) Introduction to the Program Fullprof

[36] Grice JD (2002) A solution to the crystal structures of bismutite and beyerite. Can Mineral 20:693–698

[37] Cao J, Li X, Lin H, Xu B, Chen S, Guan Q (2013) Surface acid etching $(BiO)_2CO_3$ to construct $(Bi)_2CO_3$/BiOX (X = Cl, Br, I) heterostructure for methyl orange removal under visible light. Appl Surf Sci 266:294–299

[38] Woo H, Tyson TA, Croft M, Cheong S-W, Woicik JC (2001) Correlation between the magnetic and structural properties of Ca-doped $BiMnO_3$. Phys Rev B 63:134412-1–134412-12

[39] Molak A, Ujma Z, Pilch M, Gruszka I, Pawełczyk M (2014) Resistance switching induced in $BiMnO_3$ ceramics. Ferroelectrics 464:59–71

[40] Bokov AA, Ye Z-G (2000) Phenomenological description of dielectric permittivity peak in relaxor ferroelectrics. Solid State Commun 116:105–108

[41] Bello A, Laredo E, Grimau M (2007) Comparison of analysis of dielectric spectra of PCL in the ε* and the M* formalism. J Non-Cryst Solids 353:4283–4287

[42] Molak A, Paluch M, Pawlus S, Ujma Z, Pawełczyk M, Gruszka I (2006) Properties of $(Bi_{1/9}Na_{2/3})(Mn_{1/3}Nb_{2/3})O_3$ analysed within dielectric permittivity, conductivity, electric modulus and derivative techniques approach. Phase Transit 79:447–460

[43] Molak A, Paluch M, Pawlus S (2008) Electrical properties of $Pb(Mn_{1/3}Nb_{2/3})O_3$ ceramics under hydrostatic pressure: relaxation dynamics investigation and its relation to subsystem of defects. Phys Rev B 78:34207-1–3420714

[44] Kimura T, Kawamoto S, Yamada I, Azuma M, Takano M, Tokura Y (2003) Magnetocapacitance effect in multiferroic $BiMnO_3$. Phys Rev B 67:180401-1–180401-4

[45] Bujakiewicz-Korońska R, Nalecz DM, Balanda M, Molak A, Ujma Z (2014) Electronic and magnetic properties of $(Bi_{0.5}Na_{0.5})(Mn_{0.5}Nb_{0.5})O_3$. Phase Transit 87:1096–1104